Microwave frequency ferroelectric domain imaging of deuterated triglycine sulfate crystals

D. E. Steinhauer and Steven M. Anlage[a)]
Center for Superconductivity Research and MRSEC, Department of Physics, University of Maryland, College Park, Maryland 20742-4111

(Received 9 August 2000; accepted for publication 8 November 2000)

We have used a near-field scanning microwave microscope to image domain structure and quantitatively measure dielectric permittivity and nonlinearity in ferroelectric crystals at 8.1 GHz with a spatial resolution of 1 μm. We imaged ferroelectric domains in periodically poled $LiNbO_3$, $BaTiO_3$, and deuterated triglycine sulfate (DTGS) with a signal-to-noise ratio of 7. Measurement of the permittivity and nonlinearity of DTGS in the temperature range 300–400 K shows a peak at the Curie temperature, $T_C \approx 340$ K, as well as reasonable agreement with thermodynamic theory. In addition, the domain growth relaxation time shows a minimum near T_C. We observe coarsening of ferroelectric domains in DTGS after a temperature quench from 360 to 330 K and evaluate the structure factor. © *2001 American Institute of Physics.* [DOI: 10.1063/1.1337600]

I. INTRODUCTION

Since the discovery of Rochelle salt in 1922,[1,2] ferroelectric materials have been the focus of much research, both in materials science and fundamental physics. Recently, this focus has shifted somewhat toward ferroelectric thin films, since they can be utilized in small-scale electronic devices and require lower voltages for electronically tunable devices. However, bulk crystals are still useful for research into the physics of ferroelectric materials.

For materials property measurements, a broad range of techniques exist for measuring dielectric properties[3,4] and imaging ferroelectric domains. Two of the oldest domain imaging techniques include a chemical treatment which preferentially etches domains with one direction of polarization, and the powder technique, where a colloidal suspension of charged particles, of a type which is attracted to domains with one orientation, is evaporated onto the face of the crystal.[1] Numerous other methods have been used as well. An optical microscope with crossed polarizers can be used to view domains due to the effects of optical birefringence (for 90° domains) and optical rotation (for 180° domains).[2] Laser scattering can be used, because the index of refraction of domain boundaries is different from the domain's interior.[5] Secondary electrons in scanning electron microscopy are sensitive to the surface potential variations that occur at different domains.[6] X-ray topography can be used due to variations in the Bragg angle from one domain to the next.[7] Nematic liquid crystals in a layer on top of the crystal will align with the polarization, allowing viewing of the domain structure with crossed polarizers.[8] A pyroelectric probe involves locally heating the sample with a laser and detecting the sign of the pyroelectric current.[9] Second harmonic generation of reflected light is sensitive to the direction of polarization relative to the incident beam, when the beam is at an angle to the surface.[10] Electrostatic force microscopy can be used to image domains by measuring the local sign of the piezoelectric coefficient.[11,12] Recently, near-field microwave microscopy has been used to image ferroelectric domains.[13–15]

Previously, we described the use of our near-field scanning microwave microscope to make spatially resolved, quantitative linear and nonlinear dielectric measurements at microwave frequencies.[3,4,16] In this article, we present the application of the microscope to measurements of ferroelectric materials, including imaging of domains and investigation of critical phenomena near the ferroelectric transition in deuterated triglycine sulfate (DTGS), including computation of the structure factor as a function of time after a temperature quench.

II. DESCRIPTION OF THE EXPERIMENT

Our microwave microscope consists of a resonator contained in a coaxial cable, as shown in Fig. 1. At one end of the resonator is an open-ended coaxial probe with a protruding center conductor which is held in gentle contact with the sample. The other end of the resonator is capacitively coupled to a microwave source, which supplies microwave power to the resonator. Using the reflected signal from the resonator, we can determine resonant frequency shifts Δf and quality factor Q of the microscope resonator, using a feedback circuit.[17,18] The sharp probe tip concentrates the microwave electric field at its tip, causing the microscope's resonant frequency and Q to be perturbed depending on the local properties (such as permittivity ϵ_r) of the sample. Using a physical model for the system, we convert frequency shift into the local permittivity in the sample.[3,4,16] The spatial resolution is about 1 μm.

In addition, a bias tee in the microscope resonator allows a low-frequency local electric field to be applied to the sample, permitting measurements of dielectric nonlinearity. Because no metallic structures are near the probe tip, the strength of this bias electric field is a function of the probe tip radius (which is on the order of 1 μm), rather than the

a)Electronic mail: anlage@squid.umd.edu

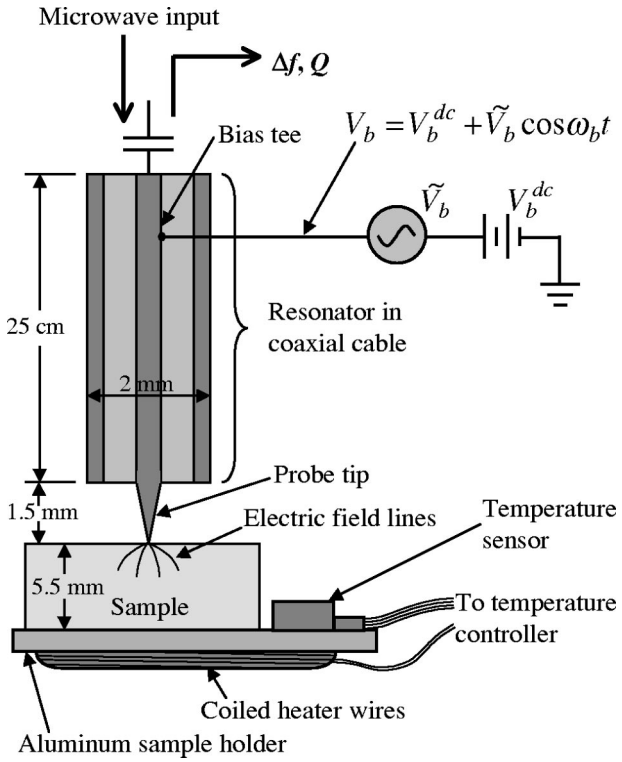

FIG. 1. Schematic of the near-field scanning microwave microscope. For simplicity, the feedback loop which produces the Δf and Q signals is not shown.

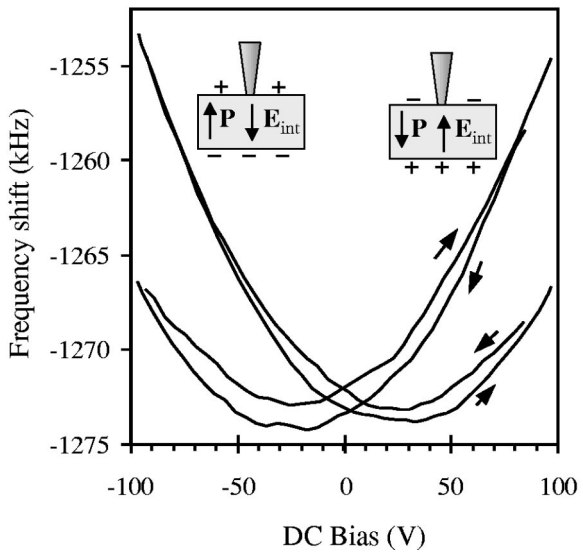

FIG. 2. Hysteresis loops at two different domains in $LiNbO_3$ at 8.1 GHz. The insets show cross-sectional schematics of domains, showing the polarization **P**, and the internal depolarization field $\mathbf{E}_{int}$ which results from the effective surface charge.

distance to ground. A heater beneath the sample allows the sample temperature to be varied in the range 300–400 K.

III. IMAGING FERROELECTRIC DOMAINS

A. Description of the measurement

To investigate the imaging of ferroelectric domains, we scanned a 0.5-mm-thick periodically poled $LiNbO_3$ crystal. The ferroelectric domains are approximately 15 μm across and are in the shape of stripes across the sample which are uniform throughout the thickness of the crystal. The polarization is perpendicular to the plane of the large face of the sample.

Figure 2 shows hysteresis loops that were acquired at two different domains. For these data, the frequency shift was acquired while the voltage bias V_b (see Fig. 1) was swept continuously in a triangle wave at a frequency 2.02 Hz, with an amplitude of 100 V, giving an average electric field of 150 kV/cm in a volume 1 μm^3 near the probe tip. Forty consecutive hysteresis loops were averaged. The frequency shift (which depends on the permittivity of the sample) changes with applied electric field due to dielectric nonlinearity.[4]

The curves in Fig. 2 have the same shape, except that they are shifted along the horizontal axis. This shifting can be explained as follows (see the insets to Fig. 2). Because of the discontinuity in the polarization **P** at the surface of the sample, an effective charge σ is at the surface of the sample, given by $\sigma = \mathbf{P} \cdot \hat{\mathbf{n}}$, where $\hat{\mathbf{n}}$ is a unit vector normal to the surface.[19] This surface charge σ produces an effective internal depolarization field $E_{int} = \sigma/\epsilon_0 = P/\epsilon_0$ in the sample, in the direction opposite to **P**. This internal electric field causes the curves shown in Fig. 2(a) to be shifted along the horizontal axis in a direction which is dependent on the local polarization. For $LiNbO_3$, with a spontaneous polarization $P_s = 0.71$ C/m^2, this would give an internal field of $E_{int} = 8.0 \times 10^5$ kV/cm. In Fig. 2, the shifts of the curves along the horizontal axis are about ± 25 V. Since the applied electric field in a 1 μm^3 volume under the probe is approximately 150 kV/cm, the total internal field in the sample is about 150 kV/cm, rather than 8.0×10^5 kV/cm. In reality, opposite charges are expected to be attracted to the surface, thereby canceling most of this internal field. Additionally, opposite charges on the surfaces of adjacent domains may cause some of the field lines to point horizontally rather than vertically, thus decreasing the magnitude of the vertical component of the internal field.

In order to acquire images of ferroelectric domains, we fix the dc voltage bias at $V_b^{dc} = 0$ V, and oscillate the bias with an amplitude $\tilde{V}_b$ at a frequency $\omega_b \sim 1$ kHz (see Fig. 1). We extract the slope (which we call df/dV) of the Δf versus bias voltage curve using a lock-in amplifier referenced at ω_b. As shown in Fig. 2, a positive slope indicates a region with polarization down, while a negative slope means the polarization is up. The magnitude of df/dV is the convolution of two effects, the dielectric nonlinearity (which changes the slope of the curves in Fig. 2), and the magnitude of the polarization (which affects the internal field and therefore shifts the curves along the horizontal axis in Fig. 2).

B. Lithium niobate

Shown in Fig. 3(a) is an image of an 80×80 μm^2 region of the $LiNbO_3$ sample. As shown in the color bar, the shades of gray indicate the derivative signal df/dV. The white areas have $df/dV < 0$, meaning the polarization is up (out of the

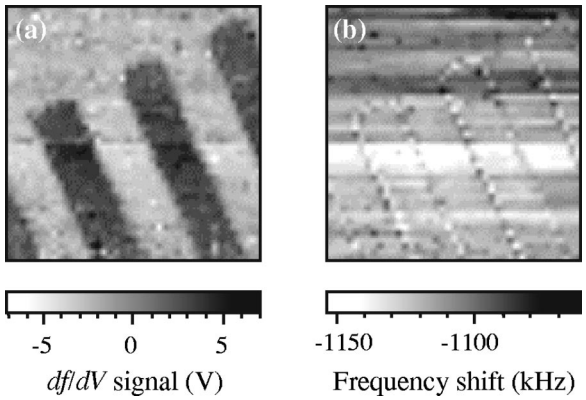

FIG. 3. Images acquired at 8.1 GHz showing ferroelectric domain structure (a) and permittivity contrast through the frequency shift of the microscope (b) in a 80×80 μm^2 region of a $LiNbO_3$ crystal.

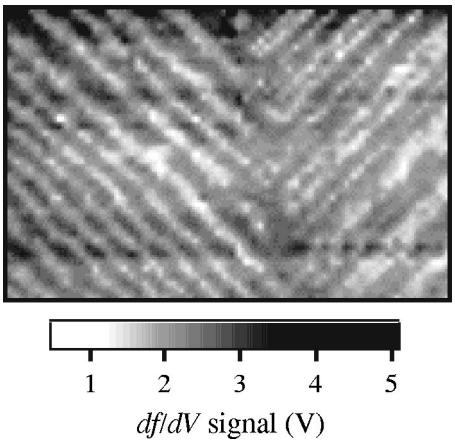

FIG. 4. Nonlinear dielectric response image acquired at 8.1 GHz showing domains in a 90×60 μm^2 region of a $BaTiO_3$ crystal.

page), while the black areas have polarization down. Images of the opposite face of the sample result in the sign of the df/dV signal being reversed, proof that this measurement is sensitive to the vertical component of polarization.

Figure 3(b) shows a frequency shift image of the same region as (a). The permittivity of different domains appears to be the same, regardless of the direction of polarization. However, the domain boundaries clearly appear in these frequency shift images. In addition, other images acquired using the microwave microscope show an increase in the microscope Q localized at the domain boundaries. Atomic force microscope images of the sample show that a 60 nm high step of width $\leqslant$200 nm exists at the domain boundaries. Thus, the change in frequency shift and increase in Q at the domain boundaries could be due to less material being near the probe tip when it approaches a downward step at domain boundaries. Similar topographic features have been observed in microwave microscope images on the surface of $PbTiO_3$.[20]

C. Barium titanate

Barium titanate, a perovskite which is tetragonal below the Curie temperature (T_C) of 390 K,[1] can be polarized along any of its three perpendicular crystal axes. Figure 4 shows a microwave microscope image of a region of a $BaTiO_3$ crystal where long, narrow domains join together near the center of the image. Because $BaTiO_3$ tends to have 90° domains rather than 180° domains, neighboring domains alternately have polarization in the horizontal and vertical directions.[1] Thus, the black regions (large df/dV) in Fig. 4 have polarization down, while the white regions (small df/dV) have horizontal polarization. The white regions in Fig. 4 with horizontal polarization have no surface charge due to the absence of a discontinuity in the normal component of the polarization at the crystal surface, and hence no normal component of internal field to cause the shifting of the curves shown in Fig. 2.

D. Deuterated triglycine sulfate

Deuterated triglycine sulfate, $(ND_2CD_2COOD)_3\,D_2SO_4$ (DTGS) has a T_C of $\sim$335 K.[21] It is an order-disorder ferroelectric with a second-order transition. The polarization is uniaxial, along the [010] axis.

Shown in Fig. 5 are domain images (df/dV) of a 5.5-mm-thick DTGS crystal, acquired at 307 K. The images show a 20×20 μm^2 region of the sample. The [010] axis is normal to the surface in these images. By applying a dc bias electric field to a ferroelectric crystal, it was possible to switch the polarization of a region of the sample, which can only be in the (010) or (010) directions. The original image of a 20×20 μm^2 region of the DTGS sample is shown in Fig. 5(a). After acquiring this image, we placed the probe at the point marked by a ''+'' in (a), and applied a bias of +70 V to the sample for about 1 min. After bringing the dc bias

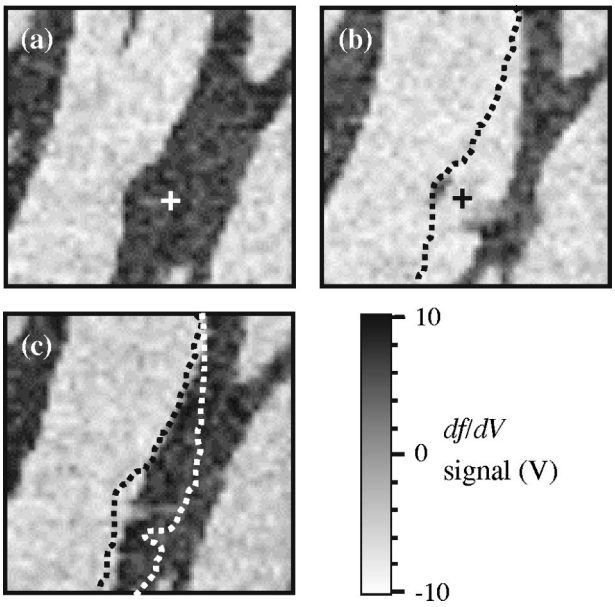

FIG. 5. Switching of a ferroelectric domain in a DTGS crystal at $T=300$ K. Images, at 8.1 GHz, are of the same 20×20 μm^2 region. After acquiring (a), a positive bias was applied at the + sign. After acquiring (b), a negative bias was applied at the + sign.

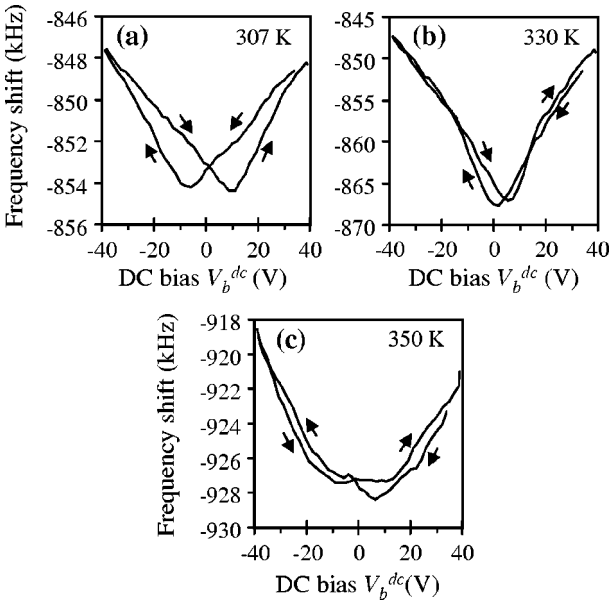

FIG. 6. Hysteresis loops of frequency shift (more negative frequency shift corresponds to larger permittivity) of DTGS at three different temperatures: (a) 307, (b) 330, and (c) 350 K. The Curie temperature is approximately 335 K.

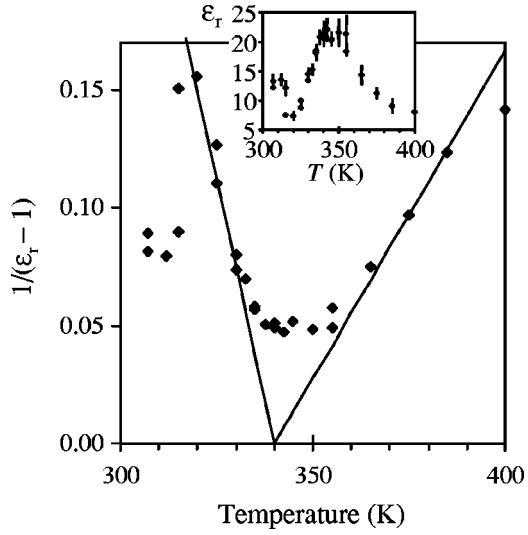

FIG. 7. Inverse electric susceptibility $1/(\epsilon_r - 1)$ vs temperature in DTGS at 8.1 GHz. The two lines are fits below and above $T_C = 340$ K. Inset: ϵ_r vs temperature.

voltage back to 0 V, we acquired the image shown in (b). The polarization in the region outlined by the dotted line has switched directions. Next, we applied a bias of -70 V to the point in (b) marked by the $+$, and after about 1 min brought the bias back to 0 V. The image in (c) shows that the region outlined by the white dotted line has once again reversed polarization to look much like the image in (a).

It is not surprising that only a small portion of the domain in Fig. 5(b) is switched by applying a bias voltage to the probe tip, since the bias electric field is concentrated over a tiny volume $\sim 1\ \mu\text{m}^3$ near the probe tip. In fact, sometimes applying an electric field leaves the domain structure unaffected. For example, when we placed the probe near the center of the white region in the middle of Fig. 5(c), and applied a bias of $+70$ V for 1 min, the resulting image was unchanged. This is probably because we were applying the electric field to an area near the center of a large domain, where switching polarization requires more energy than in a region near a domain boundary.

IV. TEMPERATURE-DEPENDENT MEASUREMENTS WITH DTGS

Figure 6 shows hysteresis loops in the permittivity at the same location on a DTGS crystal, acquired at three different temperatures, 307, 330, and 350 K. At all three temperatures, the microscope resonant frequency increases with increasing electric field magnitude, indicating that the permittivity goes down when an electric field is applied; this is the expected result.[1] At 307 K, there is a large amount of hysteresis. At 330 K, just below the Curie temperature of ~ 335 K, there is very little hysteresis. At 350 K, in the paraelectric state, there is virtually no hysteresis, and the curve has flattened out at its base. The horizontal positions of the minima in Fig. 6 give some indication of the relative magnitude of the polarization: in (a), the minima are farther apart than in (b), evidence that the polarization is larger farther below T_C. In (c), the slope of Δf vs V_b^{dc} is approximately zero at $V_b^{\text{dc}} = 0$, as expected above T_C.

A. Measurement technique

To investigate the critical behavior of the permittivity of DTGS, we converted the frequency shifts from the hysteresis loops into quantitative permittivity and tunability. Since the measurement is sensitive to both horizontal and vertical components of permittivity, we had to make an assumption about the sample permittivity tensor. At low frequency at least, the permittivity ϵ_r in the (100) and (001) directions is relatively constant in the temperature range 300–400 K at $\epsilon_r^{(100)} = 9$ and $\epsilon_r^{(001)} = 5$.[22] Thus, with the (010) axis normal to the top face of the sample, we were able to assume the horizontal component of permittivity to be constant; we took its value to be 7. Using a finite element model,[3,4,16] taking the component of ϵ_r along the (010) direction to be the unknown quantity to be measured, we were able to measure the zero-field permittivity $\epsilon_r^{(010)}$ as a function of temperature, as shown in the inset to Fig. 7. The permittivity peaks in the range 340–350 K. This is slightly above the expected Curie temperature $T_C \sim 335$ K, probably because the top surface of the 5.5-mm-thick sample is slightly cooler than the measured temperature of the heater stage (see Fig. 1).

B. Thermodynamic theory and Curie constants

Before quantitatively discussing the behavior of DTGS near T_C, we will review some of the relevant theory of ferroelectrics. Following the phenomenological thermodynamic theory of Devonshire,[2,23] for a uniaxial ferroelectric with a potential which is symmetric in polarization P, we can expand the free energy in powers of the polarization

$$F = \frac{\alpha}{2}P^2 + \frac{\gamma}{4}P^4 + \frac{\delta}{6}P^6 + F(T,X), \tag{1}$$

where α, γ, and δ are material-dependent parameters, T is the temperature, and X is stress. The electric field E is

$$E=\frac{\partial F}{\partial P}=\alpha P+\gamma P^3+\delta P^5. \tag{2}$$

For a second-order transition (such as with DTGS), $\gamma>0$, so that a double well exists in $F(P)$ below T_C and a single well above T_C. Also, the higher order term is not required for representing the transition, so we restrict ourselves to the first two terms in the expansion.

For the temperature dependence, we take

$$\alpha=\beta(T-T_C). \tag{3}$$

The relative permittivity is then

$$\frac{1}{\epsilon_r(P)-1}=\frac{\partial E}{\partial P}=\alpha+3\gamma P^2. \tag{4}$$

Above T_C, $P=0$, giving the Curie-Weiss law

$$\epsilon_r^0-1=\frac{1}{\alpha}=\frac{1}{\beta(T-T_C)}\equiv\frac{C_>}{T-T_C},\quad T>T_C, \tag{5}$$

where ϵ_r^0 is the zero-field permittivity. The parameter $C_>=1/\beta$ is the Curie constant for $T>T_C$.

The Curie constant $C_>$ can be found from our data by plotting $1/(\epsilon_r-1)$ as a function of temperature, as shown in Fig. 7. The straight lines are fits above and below T_C. The lines cross the horizontal axis at 340 K, which we take to be the temperature measured by the temperature sensor when the sample is at T_C. Because the sample is thick (5.5 mm), the top surface is expected to be at a lower temperature than that measured by the sensor, explaining why the measured T_C (340 K) is greater than the expected T_C of $\sim$335 K.[21] From the slope of the linear fit for $T>T_C$, we find the Curie constant $C_>=360$ K. Previously reported values for $C_>$ in DTGS are in the range 1900–3000 K,[24,25] 5–8 times larger than our measured value. This disagreement could be due to a variety of reasons. First, our measurement is at high frequency, which has the effect of dielectric critical slowing down (see Sec. IV C). Second, the finite size of the sample, and the fact that we are measuring the permittivity over a small volume, would suppress the peak in $\epsilon_r(T)$. Finally, the mismatched capacitor electrodes (a plane on the bottom and a sharp probe on the top) are expected to cause an internal bias field, which cannot necessarily be removed by applying an external bias. All of these effects would tend to flatten out the curve in Fig. 7(b) near T_C, forcing us to obtain the linear fits over a larger temperature range on either side of T_C.

From Eq. (2), the spontaneous polarization is

$$P_s=P|_{E=0}=-\frac{\beta(T-T_C)}{\gamma}. \tag{6}$$

Substituting Eq. (6) into Eq. (4), we get

$$\epsilon_r-1=\frac{-2}{\beta(T-T_C)},\quad T<T_C. \tag{7}$$

Thus, the Curie constant below T_C is twice that above T_C:

$$\frac{C_<}{C_>}=-2 \tag{8}$$

For many materials, such as $BaTiO_3$, Eq. (8) is accurate. However, in DTGS, due to the larger thermoelectric effect in DTGS (the thermoelectric coefficient for TGS is approximately five orders of magnitude higher than for $BaTiO_3$)[26] the constant-temperature assumption is invalid. The measurement is adiabatic rather than isothermal, requiring an additional term in Eq. (8):[25,27]

$$\frac{C_<}{C_>}=-2\left(1+\frac{\beta T_C}{2\gamma c_p}\right)\approx-2.4, \tag{9}$$

where c_p is the heat capacity per unit volume at constant polarization.

From the linear fits in Fig. 7, we find the ratio of slopes to be -2.7, in close agreement with the theoretical value of -2.4, and well within the range of values published previously, -2.3 to -4.2, based on measurements of $\epsilon_r(T)$ for frequencies below 50 kHz.[25,27]

C. Critical slowing down of dielectric response

The data in the inset to Fig. 7 flattens out near T_C, reaching a maximum of only $\epsilon_r\approx22$. This differs significantly from low-frequency data in the kilohertz range, which shows a peak in $\epsilon_r(T)$ several orders of magnitude higher, in the range 10^3-10^5.[22,25,27] Our own measurements at frequencies less than 1 MHz show a peak in $\epsilon_r(T)$ of approximately 2×10^4. We attribute the difference between kilohertz and microwave measurements of $\epsilon_r(T)$, at least in part, to dielectric critical slowing down. When the measurement period (the inverse of the measurement frequency) is shorter than the relaxation time of the polarizing distortion of the crystal lattice, the rf electric field cannot fully polarize the lattice because the ions move too slowly to keep up with the driving field. As a result, the measured susceptibility at high frequency is suppressed.

D. Dielectric nonlinearity

In addition to the linear permittivity, the behavior of DTGS near the ferroelectric transition can also be investigated by looking at dielectric nonlinearity as a function of temperature. Using hysteresis loops like those shown in Fig. 6, we can measure the dielectric nonlinearity by defining $\Delta\epsilon_r$ as the change in permittivity upon application of 40 V to the sample through the microscope tip. Shown in Fig. 8 is $\Delta\epsilon_r$ as a function of temperature. Unlike the permittivity (Fig. 7), the nonlinearity has a sharp peak, at 340 K. This value for T_C agrees with the linear fits shown in Fig. 7. Thus, we conclude that the ferroelectric transition in the DTGS sample occurs when the temperature sensor reads 340 K, which probably is higher than the actual temperature of the top surface of the sample, as explained earlier.

Our measured tunability $(\Delta\epsilon_r/\epsilon_r)$ reaches a maximum of $\sim$2.5%, which differs from measurements that involve uniform fields, such as with a parallel-plate capacitor, since the electric field in our case is nonuniform, and concentrated in a tiny volume of the sample. For example, Triebwasser[27]

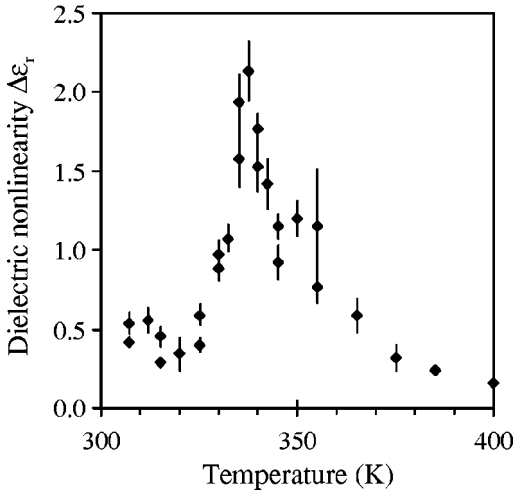

FIG. 8. Dielectric nonlinearity ($\Delta\epsilon_r$) upon application of a 40 V bias as a function of temperature in DTGS at 8.1 GHz.

measured a tunability greater than 50% for an electric field of 6 kV/cm. On the other hand, we measure a tunability of 2.5%, with an average field in a volume of 1 μm^3 beneath the probe tip of 140 kV/cm. We believe that this large difference is due to our measurement of the permittivity averaging over a larger volume than 1 μm^3. Also, our bias electric field has a component in the horizontal direction,[4] which is not expected to contribute to the measured tunability.

Taking the permittivity data similar to that shown in Fig. 6(c) for $T>T_C$, we can investigate dielectric nonlinearity in a more quantitative way by following the method of Cach *et al.*[28] Combining Eqs. (2) and (4), eliminating P, we obtain

$$\xi(E)\equiv\chi_E^3(E)+3\alpha\chi_E^2(E)-4\alpha^3=27\gamma E^2, \tag{10}$$

where $\chi_E=1/(\epsilon_r-1)$ is the electric susceptibility, and α is the zero-field electric susceptibility, both of which are measured quantities. Equation (10) gives us a quantitative relationship for the functional form for $\epsilon_r(E)$. The graph of the function $\xi(E)$ vs E^2 should be a straight line, the slope of which is proportional to the parameter γ in the free energy expansion, Eq. (1). These results are shown in Fig. 9 for temperatures from 340 to 365 K. As expected, the data appear to be along straight lines, with a slope which is somewhat independent of temperature. From the slopes of the linear fits, we calculate the parameter $\gamma=(1.6\pm0.3)\times10^{13}$ V m^5 C^{-3}. This differs from Cach's low-frequency result for TGS, $\gamma\approx6\times10^{11}$ V m^5 C^{-3} by about a factor of 25.[28] This sizeable discrepancy is probably mainly due to the suppressed ϵ_r at high frequency resulting from dielectric critical slowing down (see Sec. IV C), and the nonuniformity of the electric field around the tip.

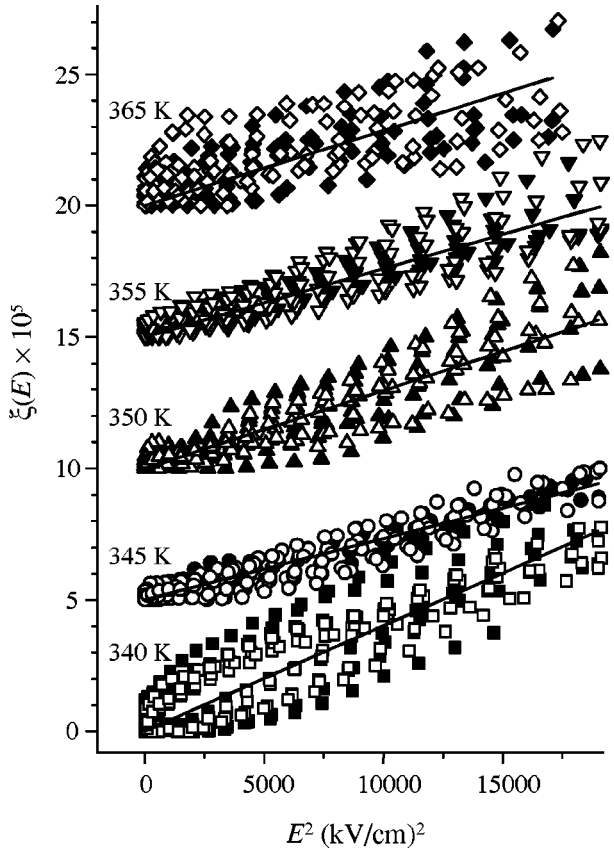

FIG. 9. The function $\xi(E)$ as a function of the square of the estimated electric field in a 1 μm^3 value below the tip for DTGS at 8.1 GHz. The data for each temperature have been offset vertically for clarity. Solid symbols are for increasing electric field, while open symbols are for decreasing electric field.

V. FERROELECTRIC DOMAIN GROWTH IN DTGS

A third way to investigate ferroelectric critical phenomena is through domain formation. When a ferroelectric crystal is cooled from above T_C to below T_C in a temperature quench, it takes a finite time for domains to nucleate and stabilize in the lowest-energy configuration.

To quantitatively measure ferroelectric domain relaxation times, we used the following procedure. First, we heated the sample, a 0.5-mm-thick DTGS crystal, to 360 K, well above T_C, and held it at that temperature for 20 min. Then we cooled it to the measurement temperature and began repeatedly imaging a 40×40 μm region of the sample. Each image took 25–35 min to complete, so data points are approximately 30 min apart. After acquiring the images, we plotted a histogram of the df/dV data for each image. Example images and histograms are shown in Fig. 10. In (a), the sample was above T_C (at 380 K for this image). No domains are present, and $df/dV\approx0$ everywhere. The histogram to the right of image (a) shows that the df/dV data are centered at about 0 V. Image (b) was acquired immediately after the sample reached 330 K, below T_C. Many long, narrow domains are visible. The histogram shows a wide peak, which does not yet appear to have separated into two peaks representing the two directions of polarization. In (c), taken 30 min later, some of the domains have joined together. Finally, in (d), acquired 210 min after (b), the narrow domains seen in (b) have joined together to form a small number of wider domains. The histogram to the right of (d) shows two distinct peaks, representing the two directions of polarization.

To compare ferroelectric domain relaxation times in DTGS as a function of temperature, we fit the histogram data

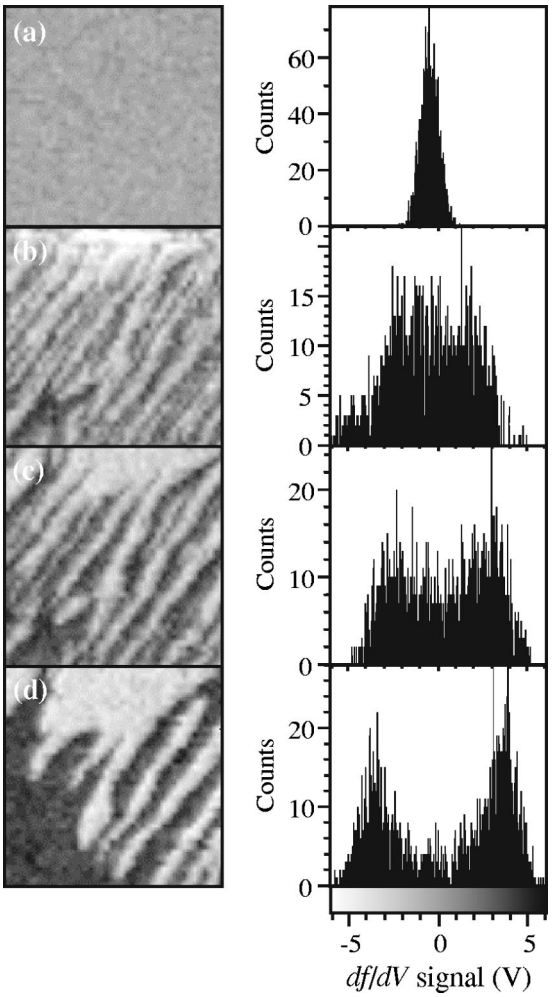

FIG. 10. Domain formation in DTGS at 330 K at 8.1 GHz. Images are of the same 40×40 μm region of the sample. (a) Image acquired with the sample at 380 K. The other three images were acquired (b) 0, (c) 30, and (d) 210 min after the sample was cooled to 330 K. The histograms to the right of the images show the gradual transition from a single peak centered at $df/dV=0$ V, to two separate peaks representing the two directions of polarization. The colorbar scale for the images is shown beneath the histograms.

for each image to a function containing the summation of two Gaussian curves with amplitudes A_1 and A_2, with $A_1>A_2$. Then, we plotted the amplitude A_1 of the largest peak for each image as a function of time, and fit this function to a decaying exponential, $A_1(t)=A_0-be^{-t/t_0}$, where A_0, b, and t_0 are fitting parameters. We took $t_0(T)$ to be the ferroelectric domain relaxation time of the crystal at temperature T.

Figure 11 shows the relaxation time t_0 as a function of temperature. The domain relaxation time appears to have a minimum near $T_C\approx335$ K, although the precise temperature of this minimum (and the minimum relaxation time) is uncertain due to the scan time (30 min) being comparable to the minimum relaxation time (15 min). This behavior can be explained using the thermodynamic model presented in Sec. IV B. The barrier between polarization states in the free energy decreases as T_C is approached from below, reaching zero at T_C. As the height of this barrier decreases, less energy is required to switch the polarization of a unit cell. Consequently, the crystal's domain structure more easily and

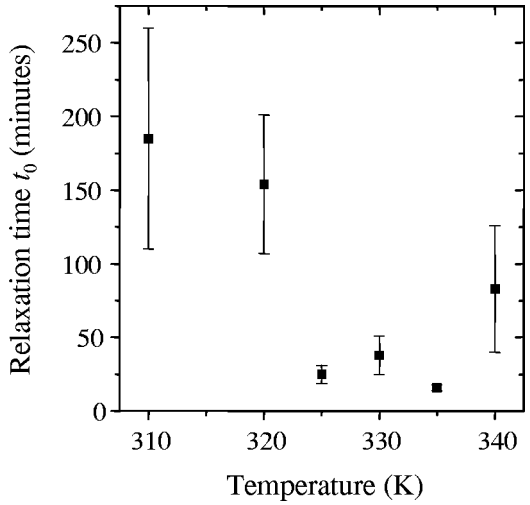

FIG. 11. Ferroelectric domain relaxation time for DTGS as a function of quench temperature, showing a minimum near $T_C\sim335$ K.

quickly relaxes to its lowest-energy state near T_C, resulting in the shorter domain relaxation times near T_C seen in Fig. 11.

The growth of domains with time after such a temperature quench through a phase transition is called coarsening[29] and can be described quantitatively using the time-dependent structure factor

$$S(|\mathbf{r}_2-\mathbf{r}_1|,t)=\langle\phi(\mathbf{r}_1,t)\phi(\mathbf{r}_2,t)\rangle, \tag{11}$$

where ϕ is the order parameter (polarization), and the average is taken over all pairs of data points $\mathbf{r}_1$ and $\mathbf{r}_2$. The structure factor is expected to scale with time with a power law dependence

$$S(|\mathbf{r}|,t)=X(|r|/t^{\nu}), \tag{12}$$

where ν is a positive exponent. In other words, the characteristic length scale of the domain correlation, $L\sim t^{\nu}$, will grow with time. In our case, we expect the df/dV signal to be a measure of the order parameter ϕ, and plot $S(r,t)$, where r is taken to be the component of $\mathbf{r}_2-\mathbf{r}_1$ perpendicular to the long axis of the domains seen in Fig. 10. The analysis of the images in Fig. 10 is shown in Fig. 12. The initial data at $t=0$ show a shorter periodicity in radial distance than the data at $t=30$, and 210 min, as expected from the scaling behavior above. Because the data at 30 and 210 min have a similar periodicity, it appears that most of the coarsening occurred during acquisition of the first two images, at $t=0$ and 30 min.

VI. CONCLUSIONS

In conclusion, we have used a near-field scanning microwave microscope to make dielectric measurements of ferroelectric materials, allowing us to image one component of ferroelectric polarization in $LiNbO_3$, $BaTiO_3$, and DTGS. The measurement of dielectric permittivity and nonlinearity at 8.1 GHz as a function of temperature showed a peak at T_C and reasonable agreement with theory. In addition, domain growth relaxation times showed a minimum near the Curie temperature.

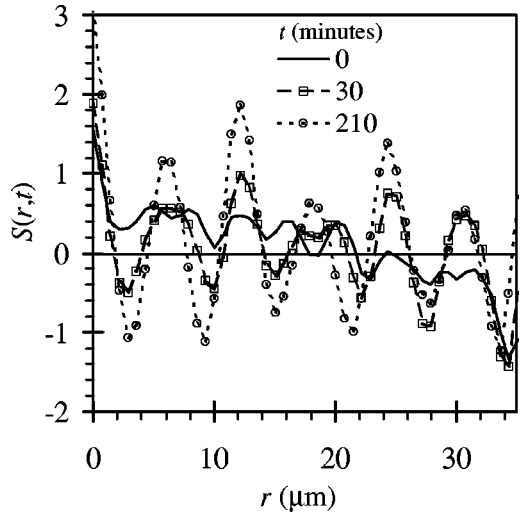

FIG. 12. The structure factor $S(r,t)$ of the df/dV images shown in Fig. 10 at three different times after a temperature quench from 380 to 330 K.

ACKNOWLEDGMENTS

The authors would like to acknowledge the assistance of Sangjin Hyun with ferroelectric domain imaging, and Hans Christen for supplying the $BaTiO_3$ crystal. This work has been supported by NSF-MRSEC Grant No. DMR-0080008, NSF Grants Nos. ECS-9632811 and DMR-9624021, and by the Maryland Center for Superconductivity Research.

[1] F. Jona and G. Shirane, *Ferroelectric Crystals* (Dover, New York, 1993).
[2] M. E. Lines and A. M. Glass, *Principles and Applications of Ferroelectric and Related Materials* (Clarendon, Oxford, 1977).
[3] D. E. Steinhauer, C. P. Vlahacos, C. Canedy, A. Stanishevsky, J. Melngailis, R. Ramesh, F. C. Wellstood, and S. M. Anlage, Appl. Phys. Lett. **75**, 3180 (1999).
[4] D. E. Steinhauer, C. P. Vlahacos, C. Canedy, A. Stanishevsky, J. Melngailis, R. Ramesh, F. C. Wellstood, and S. M. Anlage, Rev. Sci. Instrum. **71**, 2751 (2000).
[5] S. M. Shapiro, R. W. Gammon, and H. Z. Cummins, Appl. Phys. Lett. **10**, 113 (1967).
[6] N. Nakatani, Jpn. J. Appl. Phys. **12**, 1723 (1973).
[7] K. Takahashi and M. Takagi, J. Phys. Soc. Jpn. **44**, 1266 (1978).
[8] N. A. Tikhomirova, S. A. Pikin, L. A. Shuvalov, L. I. Dontsova, E. S. Popov, A. V. Shilnikov, and L. G. Bulatova, Ferroelectrics **29**, 145 (1980).
[9] N. Nakatani, K. Hayakawa, and H. Inoue, Jpn. J. Appl. Phys., Part 1 **34**, 5453 (1995).
[10] S. I. Bozhevolnyi, J. M. Hvam, K. Pedersen, F. Laurell, H. Karlsson, T. Skettrup, and M. Belmonte, Appl. Phys. Lett. **73**, 1814 (1998).
[11] L. M. Eng, H.-J. Güntherodt, G. Rosenman, A. Skliar, M. Oron, M. Katz, and D. Eger, J. Appl. Phys. **83**, 5973 (1998).
[12] C. S. Ganpule, V. Naharajan, H. Li, A. S. Ogale, D. E. Steinhauer, S. Aggarwal, E. Williams, R. Ramesh, and P. DeWolf, Appl. Phys. Lett. **77**, 292 (2000).
[13] Y. Lu, T. Wei, F. Duewer, Y. Lu, N.-B. Ming, P. G. Schultz, and X.-D. Xiang, Science **276**, 2004 (1997).
[14] Y. Cho, S. Atsumi, and K. Nakamura, Jpn. J. Appl. Phys., Part 1 **36**, 3152 (1997).
[15] Y. Cho, S. Kazuta, and K. Matsuura, Appl. Phys. Lett. **75**, 2833 (1999).
[16] D. E. Steinhauer, Ph.D. dissertation, University of Maryland, 2000.
[17] D. E. Steinhauer, C. P. Vlahacos, S. K. Dutta, F. C. Wellstood, and S. M. Anlage, Appl. Phys. Lett. **71**, 1736 (1997).
[18] D. E. Steinhauer, C. P. Vlahacos, S. K. Dutta, F. C. Wellstood, and S. M. Anlage, Appl. Phys. Lett. **72**, 861 (1998).
[19] C. Kittel, *Introduction to Solid State Physics*, 7th ed. (Wiley, New York, 1996).
[20] Y. G. Wang, M. E. Reeves, and F. J. Rachford, Appl. Phys. Lett. **76**, 3295 (2000).
[21] RAMET Ltd., Moscow, Russia (http://ramet.ad.ru). DTGS crystal, $330 \leqslant T_C \leqslant 335$ K.
[22] S. Hoshino, T. Mitsui, F. Jona, and R. Pepinsky, Phys. Rev. **107**, 1255 (1957).
[23] A. F. Devonshire, Philos. Mag. **40**, 1040 (1949).
[24] A. V. Shil'nikov, V. A. Fedorikhin, A. P. Pozdnyakov, A. V. Sopit, and L. A. Shuvalov, Phys. Solid State **41**, 977 (1999).
[25] I. M. Sil'vestrova, Sov. Phys. Crystallogr. **6**, 466 (1962).
[26] *Londolt-Börnstein: Numerical Data and Functional Relationships in Science and Technology, Ser. III*, Vol. **16**, edited by K.-H. Hellwege and A. M. Hellwege (Springer, New York, 1981).
[27] S. Triebwasser, IBM J. Res. Dev. **2**, 212 (1958).
[28] R. Cach, A. Jaśkiewicz, and R. Lamber, Acta Phys. Pol. A **62**, 249 (1982).
[29] P. M. Chaikin and T. C. Lubensky, *Principles of Condensed Matter Physics* (Cambridge University Press, Cambridge, 1995), p. 483.